Laser & Photonics Reviews

LASER & PHOTONICS REVIEWS

www.lpr-journal.org

RESEARCH ARTICLE

Spatiotemporal-Continuity-Prior-Guided Intensity Diffraction Tomography

Zihao Zhou[1,2,3] | Ning Zhou[1,2,3] | Ruizhi Zhu[1,2,3] | Jiasong Sun[1,2,3,4] | Mingyang Xu[1,2,3] | Chulmin Joo[5] | Qian Chen[1,2,3,4] | Runnan Zhang[1,2,3,4] | Chao Zuo[1,2,3,4]

[1]Smart Computational Imaging Laboratory (SCILab), School of Electronic and Optical Engineering, Nanjing University of Science and Technology, Nanjing, Jiangsu, China | [2]Smart Computational Imaging Research Institute (SCIRI) of Nanjing University of Science and Technology, Nanjing, Jiangsu, China | [3]Jiangsu Key Laboratory of Visual Sensing & Intelligent Perception, Nanjing, Jiangsu, China | [4]State Key Laboratory of Extreme Environment Optoelectronic Dynamic Measurement Technology and Instrument, Taiyuan, Shanxi, China | [5]Department of Mechanical Engineering, Yonsei University, Seoul, Republic of Korea

Correspondence: Runnan Zhang (runnanzhang@njust.edu.cn) | Chao Zuo (zuochao@njust.edu.cn)

Received: 2 March 2026 | **Revised:** 3 May 2026 | **Accepted:** 18 May 2026

Keywords: intensity diffraction tomography | label-free imaging | optical diffraction tomography

ABSTRACT

Dynamic live-cell imaging demands high spatiotemporal resolution to capture rapid intracellular processes such as organelle transport. Conventional intensity diffraction tomography (IDT) enables label-free, quantitative 3D refractive-index (RI) imaging but relies on sequential angular acquisitions, resulting in an inherent trade-off between imaging speed and reconstruction fidelity. Here, we introduce spatiotemporal-continuity-prior-guided IDT (SCP-IDT), a computational framework that breaks this trade-off by recovering intermediate 3D volumes from the same raw measurements. By leveraging the inherent spatial continuity of biological samples, SCP-IDT implements a sliding-window strategy to recombine adjacent illumination stacks for elevated imaging rates, while simultaneously employing Hessian-based regularization to mitigate RI underestimation and enhance structural fidelity beyond traditional deconvolution. To further ensure seamless 4D (xyz-t) evolution, a temporal continuity prior is imposed via a total variation constraint along the time axis, effectively bridging sequential frames. Simulations and experiments demonstrate SCP-IDT's capability to capture 4D cellular dynamics, including mitosis and intercellular material exchange with high fidelity at camera-limited speed, while maintaining incoherent diffraction-limited resolution (388 nm, 40×/0.75 NA). These capabilities position SCP-IDT as a powerful tool for quantitative kinetic analysis in drug discovery and cell biology.

1 | Introduction

Live-cell imaging provides direct access to the structural and dynamic processes underlying biological function and disease. For decades, optical microscopy has relied on fluorescence imaging as the gold standard for visualizing subcellular structures, owing to its high specificity, excellent signal-to-noise ratio and exceptional sensitivity [1–4]. However, its reliance on exogenous labeling introduces fundamental limitations: phototoxicity and photobleaching severely compromise cell viability and signal stability during prolonged observation [5, 6], while staining protocols increase experimental complexity and cost. In contrast, label-free imaging techniques exploit intrinsic optical properties of specimens, such as refractive index (RI), for image formation, eliminating the need for exogenous labeling. In recent years, label-free imaging approaches have experienced rapid develop-

Zihao Zhou and Ning Zhou have contributed equally to this work.

ment, driven by the growing demand for long-term, minimally invasive observation of live cells [7–11]. Early label-free imaging methods primarily aimed to convert the phase information of transparent specimens into visible contrast. Representative techniques include Zernike phase-contrast microscopy [12] and Nomarski differential interference contrast microscopy [13], which employ optical path designs to transform phase gradients or optical path differences into intensity variations, thereby greatly advancing the field of cellular morphological observation. Although these methods are highly effective in enhancing visual contrast, the resulting images provide qualitative information only, and are not directly suitable for precise quantitative measurements or cross-sample comparisons. To address the need for quantitative analysis, researchers have developed quantitative phase imaging (QPI) techniques that numerically reconstruct the optical phase delay induced by the sample [14, 15]. Among QPI methods, interferometric approaches, particularly digital holographic microscopy (DHM) [16–18], have played a pivotal role, offering not only high-contrast 2D phase imaging but also 3D RI reconstruction through optical diffraction tomography (ODT). However, conventional DHM typically requires mechanical rotation of the sample or objective lens [19–21], which compromises stability, limits imaging speed, and introduces alignment errors. Furthermore, the high coherence of laser illumination often produces speckle noise that degrades image fidelity.

These limitations have spurred the development of non-interferometric QPI strategies, which eliminate the need for reference beams and complex interferometric setups. In 2D, non-interferometric QPI can be broadly classified into two categories: defocus-based methods, exemplified by the transport of intensity equation [22, 23], which retrieve phase from through-focus intensity stacks; and asymmetric-illumination-based methods, such as Fourier ptychographic microscopy [24, 25] and differential phase contrast microscopy [26–28], which encode phase gradients via asymmetric or structured illumination. Building on these 2D foundations, non-interferometric QPI has recently been extended to 3D through intensity-based ODT, a framework that leverages intensity measurements under partially coherent LED illumination to achieve speckle-free, 3D RI imaging [29–31]. Intensity diffraction tomography (IDT) [32–34], a representative non-interferometric method, achieves angular scanning through oblique illumination on a single focal plane, eliminating the need for mechanical translation or rotation components. This feature makes IDT an ideal strategy for high-speed and stable live-cell imaging.

Despite its advantages, IDT faces a fundamental challenge when applied to fast dynamic biological processes. Each 3D reconstruction relies on a full set of angular measurements, meaning the temporal resolution is intrinsically constrained by the time required to complete a full acquisition cycle. As a result, only sparse temporal snapshots can be obtained, and rapid intracellular dynamics remain unresolved between consecutive acquisitions. In addition, the limited photon flux from point-source illumination often necessitates prolonged exposure to achieve sufficient signal-to-noise ratio, while high-fidelity reconstruction requires densely sampled illumination angles. These coupled requirements impose an inherent trade-off between imaging speed and reconstruction accuracy [35], limiting the ability of IDT to faithfully capture temporally continuous biological dynamics. To mitigate this conflict, several strategies have been introduced, including multiplexed illumination schemes [36–39], the incorporation of spatiotemporal smoothness priors [40–42], deep-learning-based reconstruction enhancement [43–45], and advanced scattering models tailored to dynamic cellular behavior [46]. Although these methods have shown promising results, most of them increase system complexity, impose substantial computational burdens, or rely on stringent prior-condition assumptions, which limit their practicality.

Here, we propose spatiotemporal-continuity-prior-guided intensity diffraction tomography (SCP-IDT), a high-speed computational framework that overcomes the temporal limitations of conventional IDT without hardware modification. By leveraging the inherent spatial continuity of biological samples, we employ a sliding-window strategy across the time series [47–49] to recover intermediate frames, effectively increasing temporal sampling density. This is complemented by Hessian-based spatial regularization [50–52], which mitigates RI distortion and enhances structural fidelity beyond standard reconstruction. Furthermore, we introduce a first-order temporal total variation (TV) regularizer into the volumetric inversion process to enforce continuity between sequential frames. Experimental results show that SCP-IDT achieves a 7-fold improvement in temporal sampling density while maintaining incoherent diffraction-limited resolution, establishing a practical computational route for high-fidelity 4D RI imaging with IDT.

2 | Method

2.1 | Forward Imaging Model of Intensity Diffraction Tomography

We employ an annular LED illumination board equipped with 28 high-brightness LEDs to achieve angular scanning of the sample, as shown in Figure 1a. The height of the illumination board relative to the sample stage is carefully calculated and precisely adjusted to ensure that the numerical aperture (NA) of the illumination matches exactly with that of the objective lens, thereby optimizing the spatial frequency coverage and imaging resolution.

The 3D RI distribution of the sample can be reconstructed from the scattering potential:

$$f(\mathbf{r}) = k_0^2[n_0^2 - n^2(\mathbf{r})] \tag{1}$$

where f denotes the scattering potential of the sample, $\mathbf{r} = (x, y, z)$ represents the 3D spatial coordinates, $k_0 = 2\pi/\lambda$ is the wavenumber, and n_0 and n are the refractive indices of the surrounding medium and the complex RI of the sample, respectively. Under the first-order Born approximation, Streibl [53] derived a linear relationship between the Fourier spectrum of the captured intensity images and the Fourier spectrum of the scattering potential:

$$\mathcal{F}(I) = \tilde{I} = I_0 + \tilde{f}_{\mathrm{Re}} H_P + \tilde{f}_{\mathrm{Im}} H_A \tag{2}$$

where $\mathcal{F}(\cdot) = \tilde{(\cdot)}$ denotes the Fourier transform, I is the captured image, I_0 is the zero-frequency component transmitted by the

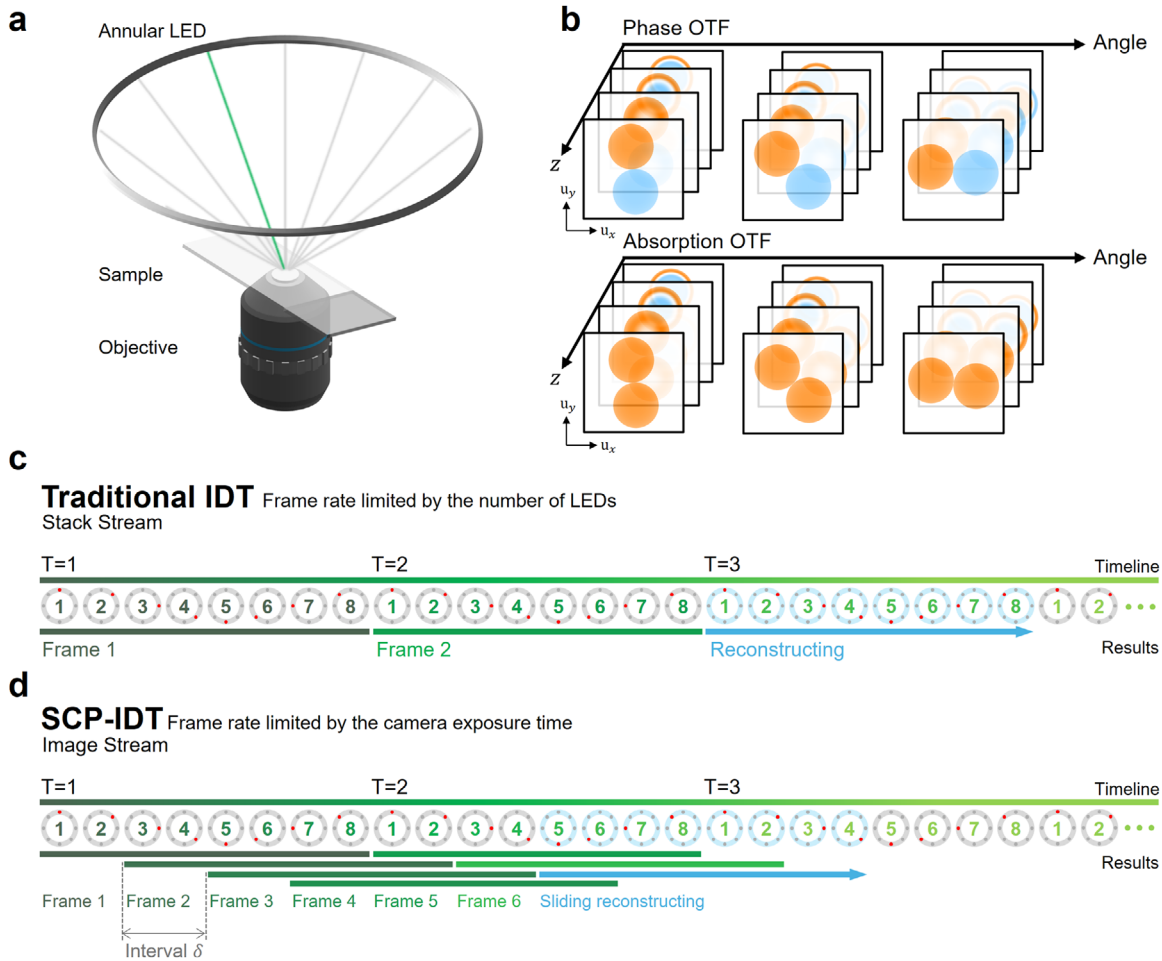

FIGURE 1 | Schematic illustration of intensity diffraction tomography and the spatiotemporal continuity prior. (a) Illumination scheme of the IDT system. (b) Cross-sectional views of the absorption optical transfer function and phase optical transfer function at different depths and illumination angles. (c,d) Comparison between the reconstruction strategies of SCP-IDT and conventional IDT, highlighting the incorporation of temporal continuity and sliding-window sampling to enhance temporal sampling density and reconstruction stability.

system, and H_P and H_A are the phase optical transfer function (POTF) and absorption optical transfer function (AOTF) of the system, respectively.

In the IDT forward imaging model, the 3D sample is discretized into a series of 2D slices, enabling axial sampling of the sample. Correspondingly, the system's transfer function is modeled in a layer-by-layer manner as shown in Figure 1b. The analytical expressions for the POTF and AOTF are given by:

$$H_P(\mathbf{u},\boldsymbol{\rho}_s)=\frac{\mathrm{i}\Delta z k_0^2}{2}\left(P(\mathbf{u}-\boldsymbol{\rho}_s)\frac{\exp\{-\mathrm{i}[\eta(\mathbf{u}-\boldsymbol{\rho}_s)-\eta_s]m\Delta z\}}{\eta(\mathbf{u}-\boldsymbol{\rho}_s)}-P(\mathbf{u}+\boldsymbol{\rho}_s)\frac{\exp\{\mathrm{i}[\eta(\mathbf{u}+\boldsymbol{\rho}_s)-\eta_s]m\Delta z\}}{\eta(\mathbf{u}+\boldsymbol{\rho}_s)}\right) \tag{3}$$

$$H_A(\mathbf{u},\boldsymbol{\rho}_s)=-\frac{\Delta z k_0^2}{2}\left(P(\mathbf{u}-\boldsymbol{\rho}_s)\frac{\exp\{-\mathrm{i}[\eta(\mathbf{u}-\boldsymbol{\rho}_s)-\eta_s]m\Delta z\}}{\eta(\mathbf{u}-\boldsymbol{\rho}_s)}+P(\mathbf{u}+\boldsymbol{\rho}_s)\frac{\exp\{\mathrm{i}[\eta(\mathbf{u}+\boldsymbol{\rho}_s)-\eta_s]m\Delta z\}}{\eta(\mathbf{u}+\boldsymbol{\rho}_s)}\right) \tag{4}$$

where P is the objective pupil function, $\mathbf{u}$ is the horizontal 2D frequency coordinate, $\eta(\mathbf{u})=\sqrt{k_0^2-|\mathbf{u}|^2}$ is the axial frequency coordinate, ρ_s is the lateral illumination wave vector, $\boldsymbol{\eta}_s(\boldsymbol{\rho}_s)=\sqrt{k_0^2-|\boldsymbol{\rho}_s|^2}$ is the axial illumination wave vector, $m\Delta z$ denotes the axial position at the m-th index under discrete sampling, and Δz is the axial sampling interval (i.e., the slice spacing).

Defining the permittivity contrast as $\Delta\epsilon(\mathbf{r})=n^2(\mathbf{r})-n_0^2=-f(\mathbf{r})/k_0^2$, the closed-form solutions of the obtained $\Delta\epsilon$ along the axial direction when using Tikhonov regularization are expressed as

$$\Delta\epsilon_{\mathrm{P}}[m]=\mathcal{F}^{-1}\left\{\frac{1}{\mathrm{Norm}}\left\{\left(\sum_l|H_A[l,m]|^2+\beta\right)\odot\left(\sum_l H_P^*[l,m]\odot G[l]\right)\left(\sum_l H_P^*[l,m]\odot H_A[l,m]\right)\odot\left(\sum_l H_A^*[l,m]\odot G[l]\right)\right\}\right\} \tag{5}$$

$$\Delta\epsilon_{\mathrm{A}}[m] = \mathcal{F}^{-1}\left\{ \frac{1}{\mathrm{Norm}}\left\{ \left(\sum_l |H_P[l,m]|^2 + \alpha \right) \odot \left(\sum_l H_A^*[l,m] \odot G[l] \right) \left(\sum_l H_A^*[l,m] \odot H_P[l,m] \right) \odot \left(\sum_l H_P^*[l,m] \odot G[l] \right) \right\} \right\} \tag{6}$$

where $\mathrm{Norm} = (\sum_l |H_P|^2 + \alpha) \odot (\sum_l |H_A|^2 + \beta) - (\sum_l H_P \odot H_A^*) \odot (\sum_l H_P^* \odot H_A)$ is the normalization term, $[m]$ denotes the m-th axial slice, $[l]$ denotes the l-th illumination angle, $\odot$ represents element-wise multiplication. For each illumination angle, a background image was acquired without the sample using the same illumination and camera settings. The raw sample image was then normalized by this background image and converted into an intensity-contrast image according to $I_l^{\mathrm{corr}} = I_l^{\mathrm{raw}}/I_l^{\mathrm{bg}} - 1$, where I_l^{raw} and I_l^{bg} are the raw sample image and the corresponding sample-free background image for the l-th illumination angle, respectively. Here $G[l]$ denotes the Fourier spectrum of this background-normalized intensity image, and α and β are the Tikhonov regularization parameters.

2.2 | Implementation of the Spatiotemporal Continuity Prior

To address the temporal resolution limitations in IDT caused by sequential acquisition cycles, we propose a reconstruction strategy guided by a spatiotemporal continuity prior imposed on the 4D scattering potential $f(\mathbf{r},t)$ (and equivalently on the RI distribution $n(\mathbf{r},t)$ through $f(\mathbf{r},t) = k_0^2[n_0^2 - n^2(\mathbf{r},t)]$). For live-cell imaging, the RI distribution $n(\mathbf{r},t)$ typically varies smoothly over time compared with its spatial variations. At the level of the macroscopic dynamics, this can be expressed as the heuristic relation

$$\left\| \frac{\partial n(\mathbf{r},t)}{\partial t} \right\| \ll \|\nabla_{\mathbf{r}} n(\mathbf{r},t)\| \tag{7}$$

which emphasizes that, over the timescale of individual illuminations and even over several acquisition cycles, the underlying 3D structure changes only gradually.

In conventional IDT, each 3D reconstruction is derived from a complete stack of intensity images acquired sequentially under multiple, uniformly distributed illumination angles L within a single acquisition cycle, as illustrated in Figure 1c. For live-cell imaging, the time intervals between individual illuminations are typically shorter than the timescales over which fine subcellular structures evolve appreciably; on this short timescale the cellular structures can be regarded as approximately stationary over a small temporal neighborhood, and the corresponding intensity measurements carry highly redundant and smoothly evolving information about $f(\mathbf{r},t)$.

Leveraging this spatiotemporal continuity, our approach relaxes the constraint of using only the fixed illumination stack within each cycle. Instead, we employ a sliding-window recombination of measurement data from neighboring acquisition cycles. By regrouping adjacent illumination stacks, we synthesize intermediate reconstruction times and thereby achieve a substantially higher effective temporal sampling density while maintaining incoherent diffraction-limited resolution. The interval parameter δ defines the sliding step between adjacent reconstruction windows, i.e., the number of newly acquired raw images by which the window advances. A smaller δ yields denser temporal sampling and stronger overlap between neighboring reconstructions, whereas a larger δ reduces temporal redundancy and the number of reconstructed volumes. In the limiting case of $\delta = 1$, the output sampling interval is bounded by the raw acquisition period.

To stably reconstruct these densely sampled 3D volumes, we explicitly encode the above physical assumption as a spatiotemporal continuity prior. In the spatial domain, we adopt a Hessian regularizer that penalizes second-order variations of the scattering potential and thus promotes spatial smoothness while preserving sharp interfaces. In the temporal domain, we introduce a temporal total variation (TV) regularizer that penalizes frame-to-frame differences and suppresses spurious temporal flicker. Together, these two terms form a joint prior on $f(\mathbf{r},t)$ that enforces continuity in both space and time and is fully consistent with the sliding-window strategy. The detailed implementation of this prior is provided in the Section S1.

Formally, for each reconstruction time index t, we seek the scattering potential $f_t(\mathbf{r}) = f(\mathbf{r},t)$ that minimizes a spatiotemporally regularized IDT cost function. Denoting by $\tilde{f}_{\mathrm{Re},t}$ and $\tilde{f}_{\mathrm{Im},t}$ the real and imaginary parts of the 3D Fourier transform $\tilde{f}_t$ of f_t, and by $H_{P,\ell,t}$ and $H_{A,\ell,t}$ the corresponding POTF and AOTF for illumination index ℓ at time t, the reconstruction problem can be written as

$$\min_{f_t} \frac{1}{2} \sum_l \left\| H_{P,l}\tilde{f}_{\mathrm{Re},t} + H_{A,l}\tilde{f}_{\mathrm{Im},t} - \tilde{I}_{l,t} \right\|_2^2 + \tau_S \mathcal{R}_H(f_t) + \tau_T \mathcal{R}_G(f_t) \tag{8}$$

where $\tilde{I}_{l,t}$ denotes the Fourier transform of the intensity image acquired under illumination l contributing to the t-th reconstruction, τ_S and τ_T are the regularization coefficients for the spatial Hessian regularizer $\mathcal{R}_H$ and the temporal TV regularizer $\mathcal{R}_G$, respectively. The implementation-specific definitions are given in Sections S1 and S2.

By jointly exploiting the spatial Hessian and temporal TV regularizers, the proposed spatiotemporal continuity prior allows SCP-IDT to recombine adjacent illumination stacks via a sliding window while maintaining high spatial fidelity and enforcing smoothly evolving, physically plausible dynamics across the reconstructed 4D RI sequence.

3 | Results

3.1 | Experimental Results of a Resolution Target Under Different Imaging Schemes

To validate the proposed method, we first evaluated how illumination sparsity affects reconstruction quality and demonstrated the efficacy of SCP-IDT in mitigating RI distortion using a static pure-phase resolution target ($360 \times 360 \times 35$ voxels, Figure 2b). All

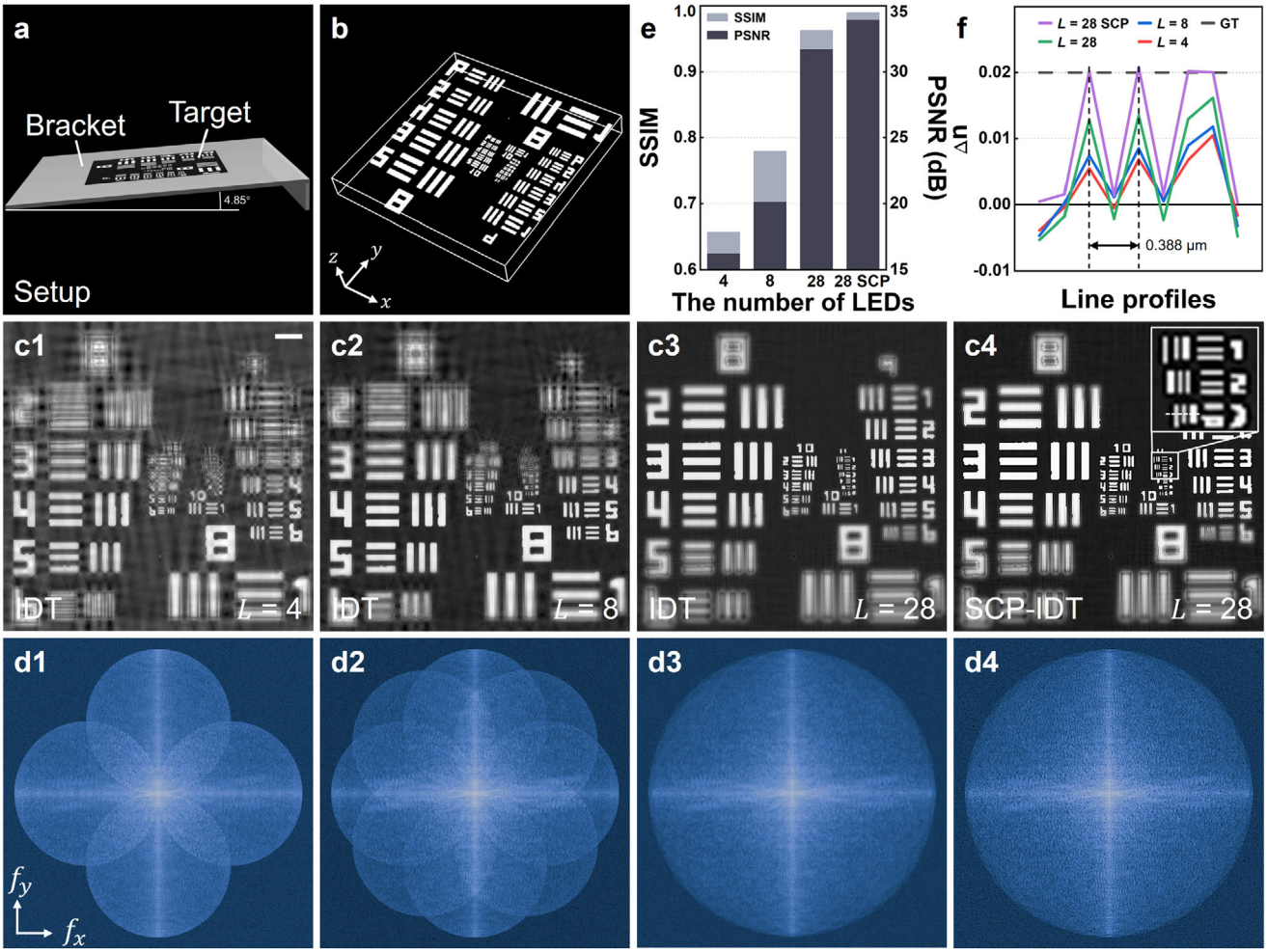

FIGURE 2 | Evaluation of illumination sparsity effects on IDT reconstruction quality. (a) Schematic diagram of sample placement. (b) Oblique pure-phase resolution target used in the experiment. (c) Comparison of reconstructed slices using conventional IDT with 4, 8, and 28 LEDs, and the proposed SCP-IDT with 28 LEDs. (d) Spatial frequency coverage under different illumination configurations. (e) Quantitative metrics calculated against the 120-LED high-density reconstruction used as the reference benchmark. (f) Line profile curves along the white dashed line in c4. Scale bar: (c1) 5 μm.

experiments were performed using a 40×/0.75 NA objective lens and green LED illumination centered at 517 nm, with a spectral bandwidth of approximately 30 nm (FWHM). We compared reconstructions derived from conventional IDT with 28, 8, and 4 LEDs against our proposed SCP-IDT using 28 LEDs. Figure 2a demonstrates the placement of the resolution target.

Figure 2c visually compares the 25th layer reconstructed under different configurations. Decreasing the number of LEDs, L, to 8 or 4 leads to severe artifacts and loss of detail. In contrast, the 28-LED configuration preserves structural details comparable to the ground truth (GT). This is supported by spectral analysis (Figure 2d), which shows that 28 LEDs provide near-complete spatial frequency coverage, representing a practical near-knee trade-off between acquisition speed and spectral completeness. However, adequate coverage does not ensure quantitative accuracy. As revealed by the line profiles in Figure 2f, conventional IDT with 28 LEDs suffers from RI underestimation compared to the true object profile. SCP-IDT (28 LEDs) significantly mitigates this distortion by incorporating Hessian-based spatial regularization, recovering RI values that align much more closely with the true object.

For quantitative assessment shown in Figure 2e, direct comparison with the defocus-free object yields uninformative metrics. Therefore, we utilized a high-density reconstruction from 120 LEDs as the reference benchmark for calculating peak signal-to-noise ratio (PSNR) and structural similarity index measure (SSIM). The results confirm that SCP-IDT achieves the highest fidelity among these configurations, effectively correcting RI inaccuracies while maintaining incoherent diffraction-limited resolution (~ 388 nm). A detailed analysis of the LED number selection is provided in Section S4.

3.2 | Simulation Results of a Smoothly Moving Cell Using IDT and SCP-IDT

The simulation was designed to systematically evaluate the imaging performance of the SCP-IDT method on a smoothly moving cell. A phase-based cellular model was constructed in 3D space (512 × 512 × 201 voxels). The model was embedded in a homogeneous medium with a RI of 1.56, while the cell body exhibited a heterogeneous RI distribution. It contained three nucleoli with varying sizes and spatial positions (RI: 1.646),

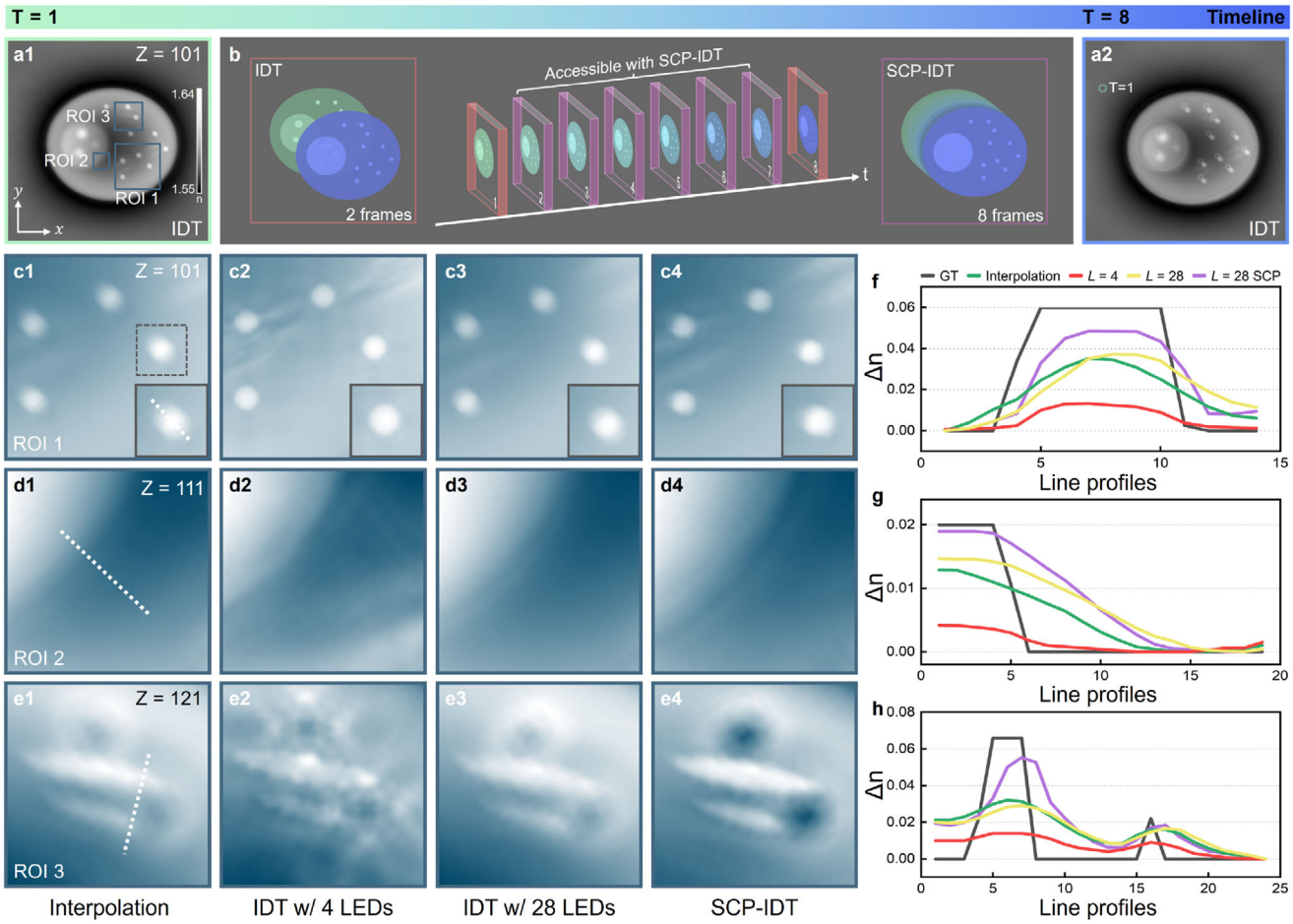

FIGURE 3 | Simulation of motion artifact suppression and structural preservation using SCP-IDT. (a) Reconstruction at the $z = 101$ plane from conventional IDT (28 LEDs) resulting in only two discrete time points. (b) Schematic illustration of the difference between SCP-IDT and conventional IDT reconstructions. (c,f) Comparison of lipid droplet reconstructions (ROI 1) at $z = 101$, showing that SCP-IDT effectively suppresses motion artifacts relative to interpolation and conventional IDT, while the 4-LED configuration avoids artifacts but exhibits pronounced RI distortion. (d,g) Reconstructions of nuclear membrane (ROI 2) at $z = 111$. (e,h) Reconstructions of chromosomes (ROI 3) at $z = 121$.

several chromosome-like spindle-shaped structures (RI: 1.666), and numerous lipid droplets (RI: 1.660), thereby realistically mimicking the structural complexity of intracellular components. To simulate dynamic behavior during imaging, the model was set to translate uniformly along the spatial diagonal direction. The motion velocity was defined such that, after every seven illumination angles, the model shifted by one voxel in both the x and y directions, thereby generating a continuously moving scene.

In this simulation, we performed SCP-IDT reconstruction using 28 LEDs and a reconstruction interval of $\delta = 4$, achieving a 7-fold increase in temporal sampling density compared to conventional IDT (i.e., high-temporal-density reconstruction equivalent to the acquisition time of a 4-LED configuration). For comparison, we also implemented a commonly used interpolation-based method to enhance temporal sampling density. Specifically, cubic spline interpolation was applied to the intensity data from three acquisition cycles around the target time point to estimate the intermediate intensity images, followed by standard reconstruction. The GT corresponds to the ideal RI distribution at the start time (t_0) of the acquisition stack, assuming instantaneous capture of all illumination angles.

Figure 3a shows the reconstruction results at the $z = 101$ plane from conventional IDT at only two discrete time points, limited by the acquisition cycle. Figure 3b schematically illustrates the difference in temporal sampling between SCP-IDT and conventional IDT, demonstrating that SCP-IDT reveals the complete motion trajectory. Specifically, Figure 3c–e presents detailed comparisons of reconstruction results using interpolation, IDT with 4-LED configuration, IDT with 28-LED configuration, and SCP-IDT across three distinct regions of interest (ROI): simulated lipid droplets at $z = 101$ (ROI 1), nuclear membrane structures at $z = 111$ (ROI 2), and chromosomes at $z = 121$ (ROI 3). Correspondingly, Figure 3f–h displays the line profiles of these methods against the GT. The results highlight distinct performance characteristics: while the 4-LED configuration is free of motion artifacts, it suffers from severe RI distortion, with values significantly underestimated compared to the GT. The interpolation-based method reconstructs the structural position more accurately with reduced temporal lag, yet it is plagued by severe motion artifacts. In contrast, SCP-IDT aligns more closely with the true spatial position than conventional IDT and exhibits significantly fewer motion artifacts than both conventional IDT and the interpolation-based method. Furthermore, the RI values

retrieved by SCP-IDT demonstrate a smaller deviation from the GT compared with conventional IDT, indicating superior quantitative accuracy. The analysis indicates that, under the 28-LED configuration, SCP-IDT achieves a favorable balance between temporal sampling density and reconstruction fidelity, outperforming both the interpolation-based approach and ultra-sparse illumination IDT methods in overall imaging performance. For clearer visual comparison and to illustrate the detailed composition of the simulated sample, the 3D rendering of the GT cell model, together with the corresponding GT slices at the locations shown in Figure 3, is provided in Section S5.

3.3 | Experimental Results of COS-7 Cells Undergoing Mitosis Using SCP-IDT

For live-cell experiments, we first applied the proposed SCP-IDT method to imaging COS-7 cells undergoing mitosis. COS-7 cells are well-suited for observing dynamic cellular processes due to their strong adherence to substrates and high mitotic activity, which allows clear visualization of the mitotic progression under standard culture conditions. Considering the characteristic timescale of intracellular dynamics, we used the same sliding reconstruction interval $\delta = 4$ for the COS-7 experiments as in the simulation. This setting provides a 7-fold increase in temporal sampling density while maintaining substantial inter-frame structural correlation. The quantitative rationale, based on the acquisition timing and reported organelle-motion scales [54], is provided in Section S3.

Figure 4b presents the reconstruction at the focal plane using SCP-IDT. Zooming into the cellular dynamics, Figure 4a1–a4 showcase the high-fidelity RI distributions of four distinct mitotic stages: prophase, metaphase, anaphase, and telophase. The clear visualization of chromosomal condensation and segregation confirms the method's excellent capability to monitor long-term physiological processes.

To explicitly demonstrate the enhancement in temporal sampling density, we tracked the rapid movement of lipid droplets in two ROIs. As shown in Figure 4c,d, conventional IDT, limited by its acquisition cycle, captures only sparse snapshots, resulting in discrete trajectory points (11 frames in c2 and 9 frames in d2). By contrast, SCP-IDT successfully recovers intermediate temporal information, reconstructing smooth, continuous motion trajectories depicted as line segments (71 frames in c1 and 57 frames in d1). This corresponds to a 7-fold increase in temporal sampling density, enabling the precise quantification of fast intracellular transport.

Furthermore, SCP-IDT provides more distinguishable structural information at defocused planes. Figure 4e,f compares the reconstruction results at axial depths of $z = +0.65$ μm and $z = -0.5$ μm, respectively. Compared with conventional IDT, which shows noticeable artifacts and weak separability between structures and background in these out-of-focus layers (Figure 4e2,f2), SCP-IDT yields clearer RI contrast and better-preserved structural edges under Hessian regularization (Figure 4e1,f1). A quantitative simulation-based analysis supporting this interpretation is provided in Section S2.

3.4 | Experimental Results of Intercellular Interaction and Organelle Transport in HeLa Cells Using SCP-IDT

We further applied SCP-IDT to investigate the intercellular interactions and intracellular dynamics of HeLa cells. Live HeLa cells exhibit complex, stochastic behaviors involving rapid organelle transport and cytoskeletal reorganization, which demand higher spatiotemporal fidelity. Figure 5a illustrates the RI distribution of the cell group. By digitally refocusing through the cellular volume, Figure 5b1–b3 resolves subcellular features with optical sectioning capabilities. High-contrast structures such as lipid droplets (Figure 5b1), fine filopodia networks (Figure 5b2), and dense nucleoli and mitochondria (Figure 5b3) are clearly distinguished at different axial depths.

To visualize the dynamic cellular interplay, Figure 5c1,c2 presents temporal color-coded projections over a duration of approximately 67 min. The spatiotemporal trajectories in Figure 5c1 reveal two distinct dynamic patterns: the directional high-speed movement of intracellular droplets (indicated by discrete color tracks) and the morphological transition from filopodia to lamellipodia, signifying active cytoskeletal remodeling. More notably, Figure 5c2 captures the formation of a tunneling nanotube (TNT) connecting two neighboring cells. This thin membrane bridge is a critical structure for intercellular communication and substance exchange.

In addition, we quantitatively analyzed the transport kinetics of a rapidly moving lipid droplet to validate the system's temporal performance. Figure 5d compares the reconstructed trajectories. The SCP-IDT method (colored line) recovers a smooth, continuous path detailing the complex maneuvering of the organelle, whereas the conventional IDT (dashed white line) yields a simplified, piecewise linear trajectory that misses subtle turns. The velocity profile in Figure 5e provides a quantitative comparison around the intermediate instance marked as point A. Within this short window, conventional IDT provides only 4 sampling points, resulting in a severe underestimation of the instantaneous velocity (0.0417 μm/s). In contrast, SCP-IDT provides 22 sampling points, revealing a higher estimated instantaneous velocity of 0.1136 μm/s. This demonstrates SCP-IDT's capability to record high-speed intracellular trafficking and transient intercellular events with reduced temporal undersampling artifacts.

4 | Conclusion and Discussion

In this work, we presented SCP-IDT, a spatiotemporal reconstruction framework designed to overcome the inherent trade-off between acquisition speed and reconstruction fidelity in conventional IDT. Rather than treating each angular stack as an isolated measurement, SCP-IDT exploits the intrinsic continuity of biological specimens across neighboring acquisition cycles. By recombining continuously acquired intensity measurements through a sliding-window strategy, the method synthetically increases the effective temporal sampling density. This data recombination is integrated into a joint spatiotemporal variational model, where Hessian-based spatial regularization enhances the quantitative RI fidelity under limited-angle conditions, and temporal TV

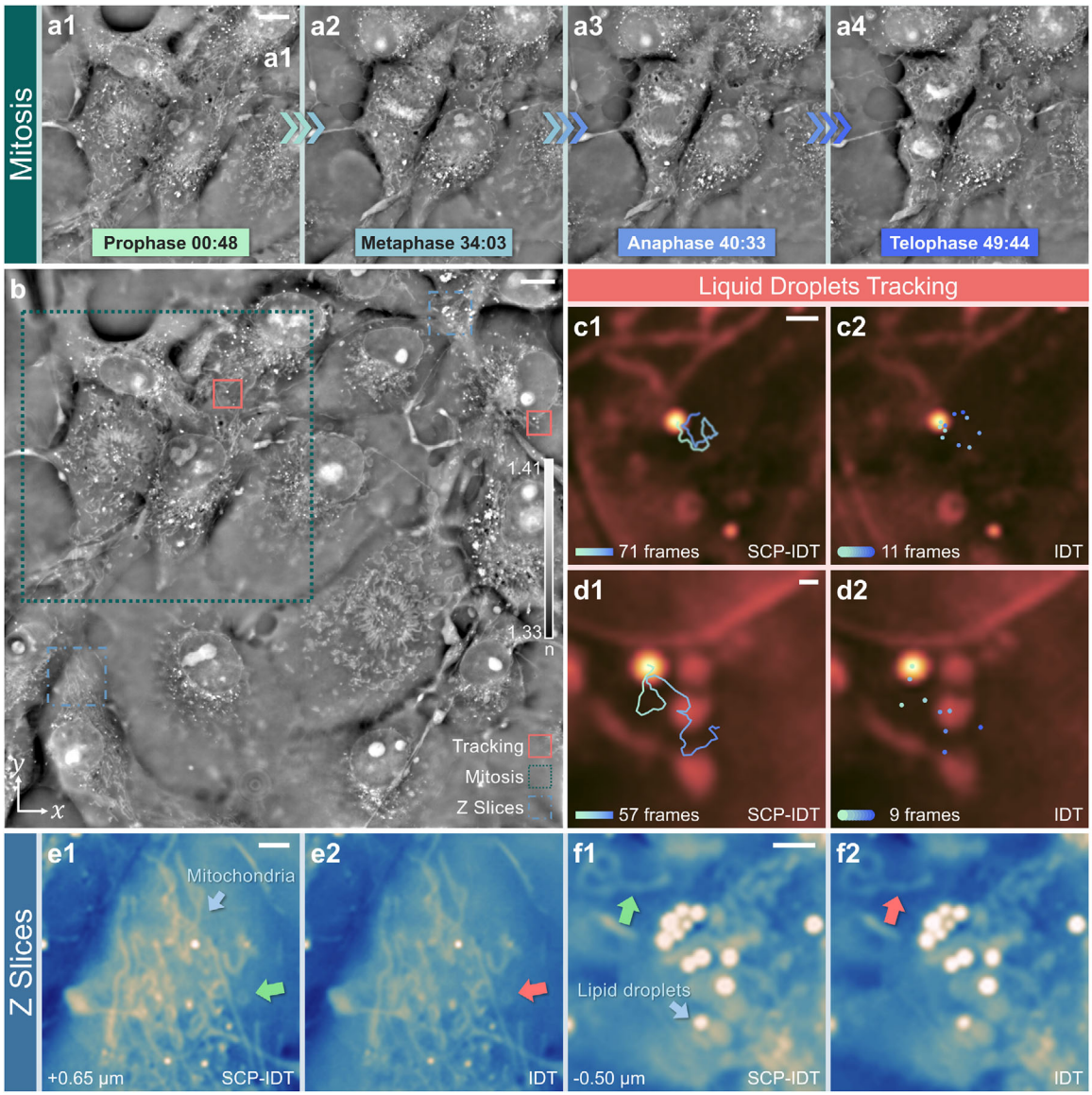

FIGURE 4 | Experimental demonstration of SCP-IDT for high-spatiotemporal-resolution imaging of mitosis in COS-7 cells. Complete results are provided in Video S1. (a) Reconstructed RI distributions of key mitotic stages within a specific ROI, capturing prophase, metaphase, anaphase, and telophase, respectively. (b) Reconstruction at the focal plane using SCP-IDT. (c,d) Comparison of dynamic tracking capabilities for lipid droplets in two different regions, highlighting the 7-fold enhancement in temporal sampling density by SCP-IDT. (e,f) Comparison of reconstruction quality at different axial depths. (e) ROI at $z = +0.65$ μm. (f) ROI at $z = -0.5$ μm. In both defocused planes, SCP-IDT (e1,f1) provides more distinguishable structural information than conventional IDT (e2,f2), mainly due to the mitigation of RI underestimation by the Hessian spatial regularization. Scale bar: (a,b) 10 μm; (c) 1 μm; (d) 0.5 μm; (e,f) 2 μm.

regularization suppresses frame-to-frame fluctuations to promote physically plausible 4D evolution.

Experimental validation across resolution targets, dynamic simulations, and live-cell imaging confirms that SCP-IDT preserves the frequency coverage of dense illumination while substantially improving RI fidelity under practical acquisition constraints. The framework recovers intermediate 3D states inaccessible to conventional IDT, outperforming both interpolation-based and ultra-sparse acquisition schemes. In live-cell studies, it enabled continuous tracking of COS-7 mitosis and resolved complex HeLa dynamics, including rapid organelle transport, cytoskeletal remodeling, and TNT formation.

Beyond algorithmic improvements, SCP-IDT offers substantial practical advantages for the broader imaging community. The framework is inherently plug-and-play and can be directly applied to previously acquired datasets, provided the original recordings follow a consistent, regularly spaced illumination sequence. This backward compatibility eliminates the need for specialized hardware or modified acquisition protocols, positioning SCP-IDT as a readily accessible computational upgrade for existing label-free microscopy workflows. By delivering enhanced temporal resolution and diffraction-limited spatial fidelity without additional experimental overhead, SCP-IDT serves as a powerful tool for quantitative kinetic analysis, with strong potential to advance phenotypic profiling, drug-response

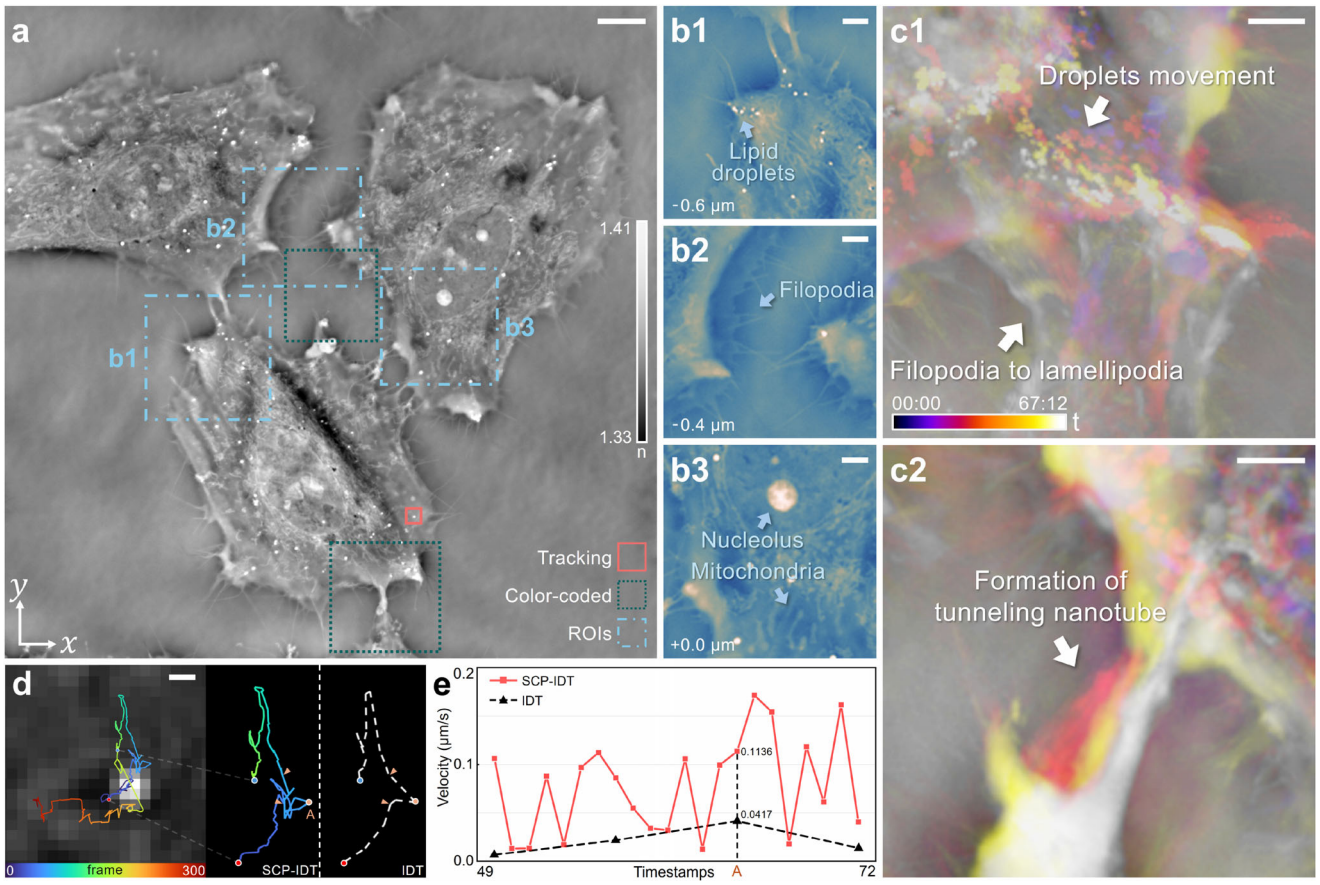

FIGURE 5 | Experimental demonstration of SCP-IDT for monitoring intercellular interactions and dynamics in HeLa cells. Complete results are provided in Video S2. (a) Representative RI distribution of HeLa cells. (b1–b3) High-resolution tomographic views at different focal depths ($z = -0.6$, -0.4, 0.0 μm), clearly resolving lipid droplets, filopodia, and nucleoli. (c1–c2) Temporal color-coded projections (0 to 67.2 min) visualizing dynamic processes. (c1) reveals the intracellular transport of droplets and the cytoskeletal reorganization from filopodia to lamellipodia. (c2) highlights the formation of a tunneling nanotube (TNT), indicating an intercellular connection. (d) Trajectory reconstruction of a lipid droplet. The SCP-IDT trace (colored) reveals complex motion details compared to the coarse IDT trace (white dashed). (e) Instantaneous velocity profile. SCP-IDT (red) captures the transient velocity spike (0.1136 μm/s) at instance A, which is missed by conventional IDT (0.0417 μm/s) due to insufficient temporal sampling. Scale bar: (a) 10 μm; (b,c) 3 μm; (d) 0.5 μm.

assessment, and the mechanistic study of dynamic intercellular processes.

Despite these advantages, SCP-IDT should be interpreted within its physical and computational limits. Each reconstructed volume is estimated from a finite temporal footprint of sequential angular measurements, and therefore represents a temporally localized estimate rather than a strictly instantaneous snapshot. When the sample displacement within this footprint becomes comparable to the characteristic feature size of interest, temporal averaging, motion-induced inconsistency, or reconstruction artifacts may arise. For faster biological dynamics [55, 56], the operating regime should therefore be adapted by reducing the number of illuminations, shortening the exposure time, improving illumination throughput, or adopting faster acquisition schemes.

From a computational perspective, SCP-IDT introduces additional iterative optimization overhead compared with closed-form conventional IDT, primarily due to the ADMM updates and the evaluation of spatiotemporal regularization terms. Quantitative benchmarks of reconstruction time, memory consumption, and convergence behavior are provided in Section S6. Future developments may combine SCP-IDT with GPU-accelerated implementation and learning-based predictive priors [57] to further reduce latency and extend the method toward faster and more complex biological dynamics. Overall, SCP-IDT provides a flexible and hardware-compatible strategy for enhancing the temporal resolving power of IDT while retaining quantitative 3D refractive-index contrast.

Acknowledgements

Z.Z. and N.Z. contributed equally to this work. This work was supported by the National Natural Science Foundation of China (62227818, 62361136588, 62305162, U21B2033, 62505136, 62575139), National Key Research and Development Program of China (2022YFA1205002, 2024YFE0101300, 2024YFF0505603, 2024YFF0505600), Fundamental Research Funds for the Central Universities (30923010206), Fundamental Research Funds for the Central Universities (2024202002), National Key Laboratory of Plasma Physics (JCKYS2024212804), and Open Research

Fund of Jiangsu Key Laboratory of Spectral Imaging & Intelligent Sense (JSGPCXZNGZ202401).

Conflicts of Interest

The authors declare no conflicts of interest.

Data Availability Statement

The data that support the findings of this study are openly available in GitHub at https://github.com/MaxZH42/SCP-IDT.

References

1. E. Betzig, G. H. Patterson, R. Sougrat, et al., "Imaging Intracellular Fluorescent Proteins at Nanometer Resolution," *Science* 313, no. 5793 (2006): 1642–1645.

2. R. M. Power and J. Huisken, "A Guide to Light-Sheet Fluorescence Microscopy for Multiscale Imaging," *Nature Methods* 14, no. 4 (2017): 360–373.

3. J. Qian, W. Xia, Y. Huang, J. Feng, Q. Chen, and C. Zuo, "Principal Component Analysis for Three-Dimensional Structured Illumination Microscopy (PCA-3DSIM)," *Light: Science & Applications* 14, no. 1 (2025): 299.

4. R. Zhang, H. Du, N. Zhou, et al., "Computational Adaptive Optics for Fluorescence Microscopy via Sparse Blind Deconvolution," *Laser & Photonics Reviews* 19 (2025): 2500032.

5. P. P. Laissue, R. A. Alghamdi, P. Tomancak, E. G. Reynaud, and H. Shroff, "Assessing Phototoxicity in Live Fluorescence Imaging," *Nature Methods* 14, no. 7 (2017): 657–661.

6. A. P. Demchenko, "Photobleaching of Organic Fluorophores: Quantitative Characterization, Mechanisms, Protection," *Methods and Applications in Fluorescence* 8, no. 2 (2020): 022001.

7. C. Zhang, Y. S. Zhang, D.-K. Yao, Y. Xia, and L. V. Wang, "Label-Free Photoacoustic Microscopy of Cytochromes," *Journal of Biomedical Optics* 18, no. 2 (2013): 020504–020504.

8. M. Ji, D. A. Orringer, C. W. Freudiger, et al., "Rapid, Label-Free Detection of Brain Tumors with Stimulated Raman Scattering Microscopy," *Science Translational Medicine* 5, no. 201 (2013): 201ra119–201ra119.

9. C. Ounkomol, S. Seshamani, M. M. Maleckar, F. Collman, and G. R. Johnson, "Label-Free Prediction of Three-Dimensional Fluorescence Images from Transmitted-Light Microscopy," *Nature Methods* 15, no. 11 (2018): 917–920.

10. K. Klein, A. M. Gigler, T. Aschenbrenner, et al., "Label-Free Live-Cell Imaging with Confocal Raman Microscopy," *Biophysical Journal* 102, no. 2 (2012): 360–368.

11. R. Zhang, N. Zhou, H. Tang, et al., "High-Speed Multi-Modal Extended Depth-of-Field Microscopy with an Electrically Tunable Lens," *Laser & Photonics Reviews* 18, no. 4 (2024): 2300770.

12. F. Zernike, "Phase Contrast, a New Method for the Microscopic Observation of Transparent Objects Part II," *Physica* 9, no. 10 (1942): 974–986.

13. R. Allen and G. David, "The Zeiss-Nomarski Differential Interference Equipment for Transmitted-Light Microscopy," *Zeitschrift für Wissenschaftliche Mikroskopie und Mikroskopische Technik* 69, no. 4 (1969): 193–221.

14. E. Cuche, F. Bevilacqua, and C. Depeursinge, "Digital Holography for Quantitative Phase-Contrast Imaging," *Optics Letters* 24, no. 5 (1999): 291–293.

15. G. Popescu, *Quantitative Phase Imaging of Cells and Tissues* (McGraw-Hill, 2011).

16. S. Shan Kou and C. J. Sheppard, "Imaging in Digital Holographic Microscopy," *Optics Express* 15, no. 21 (2007): 13640–13648.

17. X. Yu, J. Hong, C. Liu, and M. K. Kim, "Review of Digital Holographic Microscopy for Three-Dimensional Profiling and Tracking," *Optical Engineering* 53, no. 11 (2014): 112306–112306.

18. M. K. Kim, "Principles and Techniques of Digital Holographic Microscopy," *SPIE Reviews* 1, no. 1 (2010): 018005.

19. W. Choi, C. Fang-Yen, K. Badizadegan, et al., "Tomographic Phase Microscopy," *Nature Methods* 4, no. 9 (2007): 717–719.

20. C. Depeursinge, N. Pavillon, J. Kühn, T. Colomb, and P. Marquet, "Refractive Index Tomography by Digital Holographic Microscopy," in *Digital Holography and Three-Dimensional Imaging* (Optica Publishing Group, 2008), DTuC3.

21. Y. Cotte, F. Toy, P. Jourdain, et al., "Marker-Free Phase Nanoscopy," *Nature Photonics* 7, no. 2 (2013): 113–117.

22. C. Zuo, Q. Chen, W. Qu, and A. Asundi, "Noninterferometric Single-Shot Quantitative Phase Microscopy," *Optics Letters* 38, no. 18 (2013): 3538–3541.

23. C. Zuo, Q. Chen, W. Qu, and A. Asundi, "High-Speed Transport-of-Intensity Phase Microscopy with an Electrically Tunable Lens," *Optics Express* 21, no. 20 (2013): 24060–24075.

24. G. Zheng, R. Horstmeyer, and C. Yang, "Wide-Field, High-Resolution Fourier Ptychographic Microscopy," *Nature Photonics* 7, no. 9 (2013): 739–745.

25. F. Xu, Z. Wu, C. Tan, et al., "Fourier Ptychographic Microscopy 10 Years On: A Review," *Cells* 13, no. 4 (2024): 324.

26. D. Hamilton and C. Sheppard, "Differential Phase Contrast in Scanning Optical Microscopy," *Journal of Microscopy* 133, no. 1 (1984): 27–39.

27. L. Tian and L. Waller, "Quantitative Differential Phase Contrast Imaging in an LED Array Microscope," *Optics Express* 23, no. 9 (2015): 11394–11403.

28. Y. Fan, J. Sun, Q. Chen, J. Zhang, and C. Zuo, "Wide-Field Anti-Aliased Quantitative Differential Phase Contrast Microscopy," *Optics Express* 26, no. 19 (2018): 25129–25146.

29. J. M. Soto, J. A. Rodrigo, and T. Alieva, "Label-Free Quantitative 3D Tomographic Imaging for Partially Coherent Light Microscopy," *Optics Express* 25, no. 14 (2017): 15699–15712.

30. P. Müller, M. Schürmann, and J. Guck, "The Theory of Diffraction Tomography," *arXiv Preprint arXiv:1507.00466* (2015).

31. Z. Zhou, R. Zhang, N. Zhou, Q. Chen, and C. Zuo, "Multi-Modal Transport of Intensity Diffraction Tomography Microscopy with an Electrically Tunable Lens," *Biomedical Optics Express* 16, no. 2 (2025): 837–848.

32. R. Ling, W. Tahir, H.-Y. Lin, H. Lee, and L. Tian, "High-Throughput Intensity Diffraction Tomography with a Computational Microscope," *Biomedical Optics Express* 9, no. 5 (2018): 2130–2141.

33. N. Zhou, R. Zhang, R. Zhu, et al., "Adaptive Optics-Assisted Long-Term 3D Fluorescence and Intensity Diffraction Tomography for High Spatiotemporal Resolution Cellular Imaging," *Laser & Photonics Reviews* 19 (2025): 2402196.

34. R. Zhu, W. Zou, R. Zhang, et al., "Efficient Misalignment Correction for Annular LED Arrays in Intensity Diffraction Tomography," *Optics Letters* 50, no. 9 (2025): 2880–2883.

35. J. Li, A. Matlock, Y. Li, Q. Chen, C. Zuo, and L. Tian, "High-Speed in Vitro Intensity Diffraction Tomography," *Advanced Photonics* 1, no. 6 (2019): 066004–066004.

36. A. Matlock and L. Tian, "High-Throughput, Volumetric Quantitative Phase Imaging with Multiplexed Intensity Diffraction Tomography," *Biomedical Optics Express* 10, no. 12 (2019): 6432–6448.

37. Y. Fan, J. Sun, Q. Chen, X. Pan, M. Trusiak, and C. Zuo, "Single-Shot Isotropic Quantitative Phase Microscopy Based on Color-Multiplexed Differential Phase Contrast," *APL Photonics* 4, no. 12 (2019): 121301.

38. N. Zhou, J. Li, J. Sun, et al., "Single-Exposure 3D Label-Free Microscopy Based on Color-Multiplexed Intensity Diffraction Tomography," *Optics Letters* 47, no. 4 (2022): 969–972.

39. L. Tian, X. Li, K. Ramchandran, and L. Waller, "Multiplexed Coded Illumination for Fourier Ptychography with an LED Array Microscope," *Biomedical Optics Express* 5, no. 7 (2014): 2376–2389.

40. Y. Gao and L. Cao, "Motion-Resolved, Reference-Free Holographic Imaging via Spatiotemporally Regularized Inversion," *Optica* 11, no. 1 (2024): 32–41.

41. P. Bohra, T.-A. Pham, Y. Long, J. Yoo, and M. Unser, "Dynamic Fourier Ptychography with Deep Spatiotemporal Priors," *Inverse Problems* 39, no. 6 (2023): 064005.

42. M. Sun, K. Wang, Y. N. Mishra, S. Qiu, and W. Heidrich, "Space-Time Fourier Ptychography for In Vivo Quantitative Phase Imaging," *Optica* 11, no. 9 (2024): 1250–1260.

43. R. Cao, N. S. Divekar, J. K. Nunez, S. Upadhyayula, and L. Waller, "Neural Space–Time Model for Dynamic Multi-Shot Imaging," *Nature Methods* 21, no. 12 (2024): 2336–2341.

44. A. Sinha, J. Lee, S. Li, and G. Barbastathis, "Lensless Computational Imaging Through Deep Learning," *Optica* 4, no. 9 (2017): 1117–1125.

45. M. Priessner, D. C. Gaboriau, A. Sheridan, et al., "Content-Aware Frame Interpolation (CAFI): Deep Learning-Based Temporal Super-Resolution for Fast Bioimaging," *Nature Methods* 21, no. 2 (2024): 322–330.

46. J. Kim and S. Chowdhury, "Space-Time Inverse-Scattering of Translation-Based Motion," *Optica* 12, no. 5 (2025): 643–653.

47. Y. Ma, D. Li, Z. J. Smith, D. Li, and K. Chu, "Structured Illumination Microscopy with Interleaved Reconstruction (SIMILR)," *Journal of Biophotonics* 11, no. 2 (2018): e201700090.

48. J. Wu, Z. Lu, D. Jiang, et al., "Iterative Tomography with Digital Adaptive Optics Permits Hour-Long Intravital Observation of 3D Subcellular Dynamics at Millisecond Scale," *Cell* 184, no. 12 (2021): 3318–3332.

49. Y. Fu, Y. Hou, Q. Liang, et al., "Triangle-Beam Interference Structured Illumination Microscopy," *Nature Photonics* 19 (2025): 1122–1131.

50. T. Sun, N. Sun, J. Wang, and S. Tan, "Iterative CBCT Reconstruction Using Hessian Penalty," *Physics in Medicine & Biology* 60, no. 5 (2015): 1965.

51. X. Huang, J. Fan, L. Li, et al., "Fast, Long-Term, Super-Resolution Imaging with Hessian Structured Illumination Microscopy," *Nature Biotechnology* 36, no. 5 (2018): 451–459.

52. L. Zhang, Y. Wang, T. Liu, et al., "Hessian Intensity-Only Diffraction Tomography for 3D Refractive Index Reconstruction," *Optics and Lasers in Engineering* 195 (2025): 109285.

53. N. Streibl, "Three-Dimensional Imaging by a Microscope," *Journal of the Optical Society of America A* 2, no. 2 (1985): 121–127.

54. A. M. Valm, S. Cohen, W. R. Legant, et al., "Applying Systems-Level Spectral Imaging and Analysis to Reveal the Organelle Interactome," *Nature* 546, no. 7656 (2017): 162–167.

55. D. Dong, X. Huang, L. Li, et al., "Super-Resolution Fluorescence-Assisted Diffraction Computational Tomography Reveals the Three-Dimensional Landscape of the Cellular Organelle Interactome," *Light: Science & Applications* 9, no. 1 (2020): 11.

56. P. Balondrade, V. Barolle, N. Guigui, et al., "Multi-Spectral Reflection Matrix for Ultrafast 3D Label-Free Microscopy," *Nature Photonics* 18, no. 10 (2024): 1097–1104.

57. W. Wang, Q. Wang, K. Zheng, et al., "Framer: Interactive Frame Interpolation," *arXiv Preprint arXiv:2410.18978* (2024).

Supporting Information

Additional supporting information can be found online in the Supporting Information section.

Supporting File 1: lpor71377-sup-0001-SuppMat.pdf.
Supporting File 2: lpor71377-sup-0002-VideoS1.mp4.
Supporting File 3: lpor71377-sup-0003-VideoS2.mp4.
Supporting File 4: lpor71377-sup-0004-VideoS3.mp4.